Density profiles of loose and collapsed cohesive granular structures generated by ballistic deposition

Dirk Kadau and Hans J. Herrmann
Institute for Building Materials, ETH Zurich, CH-8093 Zürich, Switzerland
(Received 25 October 2010; revised manuscript received 15 December 2010; published 2 March 2011)

Loose granular structures stabilized against gravity by an effective cohesive force are investigated on a microscopic basis using contact dynamics. We study the influence of the granular Bond number on the density profiles and the generation process of packings, generated by ballistic deposition under gravity. The internal compaction occurs discontinuously in small avalanches and we study their size distribution. We also develop a model explaining the final density profiles based on insight about the collapse of a packing under changes of the Bond number.

DOI: 10.1103/PhysRevE.83.031301 PACS number(s): 45.70.Mg, 47.57.−s, 83.80.Hj

I. INTRODUCTION

Loose granular packings, metastable granular structures, and fragile granular networks play an important role in a wide range of scientific disciplines, such as collapsing soils [1–4], fine powders [5], or complex fluids [6,7]. In collapsing soils, without any doubt there is a metastable or fragile granular network involved [1–3,8,9]. A similar failure behavior can be found in colloidal gels [10] and snow [11,12]. But also powders have, in most cases, an effective cohesive force, for example, due to a capillary bridge between the particles or van der Waals forces (important when going to very small grains, e.g., nanoparticles), leading to the formation of loose and fragile granular packings [5,8,9,13]. In many complex fluids a fragile or metastable network of colloids or grains is believed to be the essential ingredient for the occurrence of shear thickening [6] or yield stress behavior [7].

The general feature of such fragile networks is that they can collapse or compact under the effect of an applied load [9,11,13]. This load can be an external load or exerted internally by a force acting on all particles within the structure. This "internal collapse" is important in different applications such as cake formation of filter deposits [14–16], where the compaction force in most situations is the drag force exerted on the grains by the flow, which is typically porosity dependent [17]. The structure's own weight leads to compaction of snow after deposition [18] and during aging [19,20] or to sediment compaction [21–23]. In all cases, typically a depth-dependent porosity is observed and quantified by continuum descriptions [15,16,18,21–23]. In most cases the details of the porosity profile are influenced by a combination of different mechanical and chemical processes [15,21]. It is well known that the porosity of a structure is of major importance for its mechanical properties [11,21,24,25], in filtration processes [26], and for its chemical properties like catalytic activity [27]. The aim of this paper is to study the microscopic processes, that is, on the grain scale, for these internal compaction processes. For this, we investigate the compaction due to gravity in a simplified model system of grains held together by cohesive bonds. We analyze how the density profiles depend on the granular Bond number, that is, the ratio of cohesive force to gravity, and the influence of the dynamics of deposition and collapse. As discussed above, loose structures are generated in nature, industrial application, experiments, or simulation by different processes. Here, we focus on ballistic deposition. However, we expect the findings of this paper to be of relevance for all systems involving compaction due to the particles' own weight. After a description of the simulation model and a brief discussion of possible experimental realizations in Sec. II, we first study the resulting density profiles when gravity acts during deposition, in particular, the influence of the granular Bond number (Sec. III). To understand the shape of the density profiles, in Sec. IV we study the role of the dynamics of the collapse occurring in small avalanches. We study the average "avalanche profile," defined here as the average distance a particle moves downward after being deposited depending on its height. We observe characteristic profiles that can be used to relate the final density profile to the deposition density, given by the number of deposited particles per unit volume (Sec. V). To understand this phenomenological profile we study a simpler system where first all particles are deposited, followed by the collapse of the whole structure, leading to an even simpler profile (Sec. VI). Our calculations yield that this linear profile is obtained in all processes where a homogeneous initial configuration is collapsed or compacted to a homogeneous final state. In Sec. VII we show that the phenomenological obtained avalanche profile obtained in Sec. III can be derived from the linear avalanche profiles of the homogeneous collapse.

II. DESCRIPTION OF SIMULATION MODEL

The dynamical behavior of the system during generation is modeled with a particle-based method. Here we use a two-dimensional variant of contact dynamics, originally developed to model compact and dry systems with lasting contacts [28–31]. The absence of cohesion between particles can only be justified in dry systems on scales where the cohesive force is weak compared to the gravitational force on the particle, that is, for dry sand and coarser materials, which can lead to densities close to that of random dense packings. However, an attractive force plays an important role in the stabilization of large voids [32], leading to highly porous systems, as, for example, in fine cohesive powders, in particular, when going to very small grain diameters. Also, for contact dynamics a few simple models for cohesive particles are established [32–35]. Here we consider the bonding between two particles in terms of a cohesion model with a constant attractive force F_c acting within a finite range d_c, so that for the opening of a contact a finite-energy barrier $F_c d_c$ must be overcome. In addition, we implement Coulomb and rolling friction between two particles in contact, so that large pores can be stable [32,36–39].

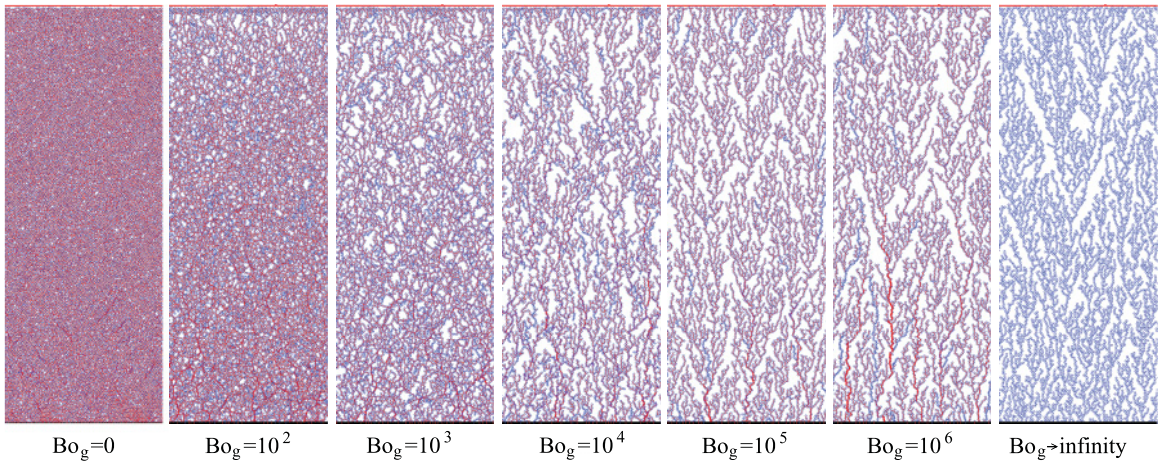

FIG. 1. (Color online) Final structures achieved by the deposition and collapse process for different granular Bond numbers Bo_g. In addition to the particles, compressive forces are illustrated by red (dark-gray) lines connecting the center of masses between the particles. In the case of $\mathrm{Bo}_g \to \infty$ no forces are present, as is realized in the simulations by switching off gravity.

To generate the loose structure we use ballistic deposition where each deposited particle, chosen at random horizontal position, is attached to the structure at maximal possible height with zero velocity. At the same time we allow for all particles to move, which can lead to a partial collapse of the structures due to gravity [8,9,13,40]. The structure is deposited on a flat surface, that is, a wall at the bottom. We use periodic boundaries in the horizontal direction to avoid effects of side walls, like the Janssen effect. During this process the time interval between successive depositions crucially determines the structure and density profiles of the final configurations. Here we focus on the two extreme cases of very large time intervals, that is, the system can fully relax after each deposition of a single grain, and vanishing time interval, that is, the collapse of the systems happens after the deposition process is complete. In the first case the interval is chosen large enough to let the system compactify and relax due to the additional weight of the deposited grain. This is verified, on one hand, by checking that the final density is independent on the time interval and, on the other hand, by monitoring the dynamics of the process. Having no time between depositions, in practice, means that we first perform pure ballistic deposition [41,42] and then switch on the full particle dynamics, leading to a collapse of the system due to gravity. Experimentally, the two cases can be realized in a Hele-Shaw cell [43–45] which can be tilted to effectively change gravity

In the slow deposition process, the cell is simply filled slowly in an upright position so that full gravity acts on the grains. In the other case the Hele-Shaw cell will be almost horizontal, so that the grains can be filled in with nearly vanishing gravity, and then the cell is tilted so that gravity can fully act on the grains, leading to an abrupt collapse of the structure.

III. DENSITY PROFILES WHEN GRAVITY ACTS DURING DEPOSITION

In this section we analyze the density profiles for the case of time intervals between successive depositions long enough to allow the systems to relax under the effect of gravity as described in the previous section. It is expected that the density and the characteristics of the density profiles are mainly determined by the ratio of the cohesive force F_c to gravity F_g, typically defined as the granular Bond number, $\mathrm{Bo}_g = F_c/F_g$ [46,47]. Obviously the case $\mathrm{Bo}_g = 0$ corresponds to the cohesionless case, whereas for $\mathrm{Bo}_g \to \infty$, gravity is negligible. A similar dimensionless quantity had been identified as the most important parameter in previous studies on compaction of cohesive powders [32,36,48].

In the following, we use monodisperse systems with a friction coefficient $\mu = 0.3$ and a rolling friction coefficient of $\mu_r = 0.1$ (in units of particle radii). The effect of varying these parameters is also studied in an exemplary fashion and is discussed later. Typically the values of the density can depend on these parameters as shown in Ref. [37], whereas the qualitative behavior does not change. Figure 1 shows the final structures obtained for different values of granular Bond number ranging from 0 to 10^6. Also, the limit of infinite Bond number is shown, leading to pure ballistic deposition [42], which has already been well studied. For small Bond numbers, here represented by $\mathrm{Bo}_g = 0$, the system typically reaches a random close packing, which also has been studied intensively in the past. Note that our case of monodisperse particles typically leads in dense packings to crystallization effects, which could be avoided by using a small polydispersity. As our focus in this paper is on looser structures where this effect is not very important, we prefer the monodisperse system to keep the model as simple as possible. In the intermediate range of Bond numbers the density varies between the two limiting values.

Plotting the density profile depending on the vertical position y (Fig. 2) provides a more quantitative analysis. It can be seen that in the two limiting cases ($\mathrm{Bo}_g = 0$ and $\mathrm{Bo}_g \to \infty$) the density is constant. For an infinite Bond number this can be explained easily, as no collapse occurs and the density profile is that of a ballistic deposition and, thus, constant [41,42]. For the noncohesive case a close packing is expected, also leading to a constant density. This is discussed again in more detail later. In

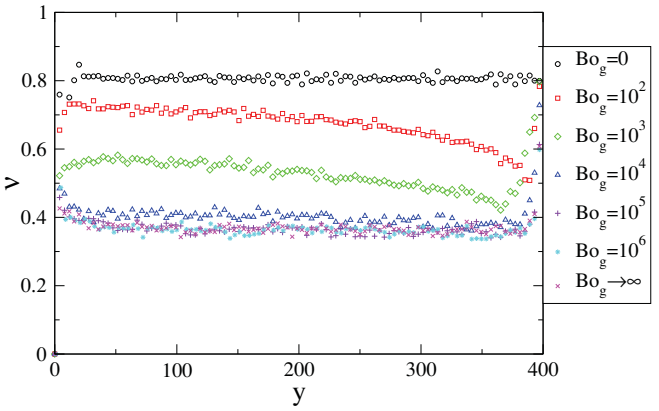

FIG. 2. (Color online) Density profiles for different granular Bond numbers Bo_g (cf. Fig. 1). Here, the volume fraction ν is plotted. In this case the volume fraction is measured in thin slices of a given width (here, 3.97 particle radii) at varying height y. For $\mathrm{Bo}_g = 0$ no cohesion is active and random close packing is reached. In the limit $\mathrm{Bo}_g \to \infty$ the system does not collapse at all, and the simple ballistic deposition case [42] is obtained.

the intermediate range the density decreases with increasing height. This is a result of the generation process where the fragile structure is partially collapsed due to the weight of the added particles, which happens discontinuously in relatively small avalanches as discussed in more detail in Sec. IV.

Knowing that the density depends on vertical position, a general dependence of the total density on the Bond number cannot easily be defined. Instead, for a given system size as in Fig. 2 the density at a fixed position can be measured. In Fig. 3 the averaged density in the lower half excluding the region very close to the bottom is shown versus the granular Bond number. The density varies between the two limiting cases $\mathrm{Bo}_g = 0$ and $\mathrm{Bo}_g \to \infty$. Note that the Bond

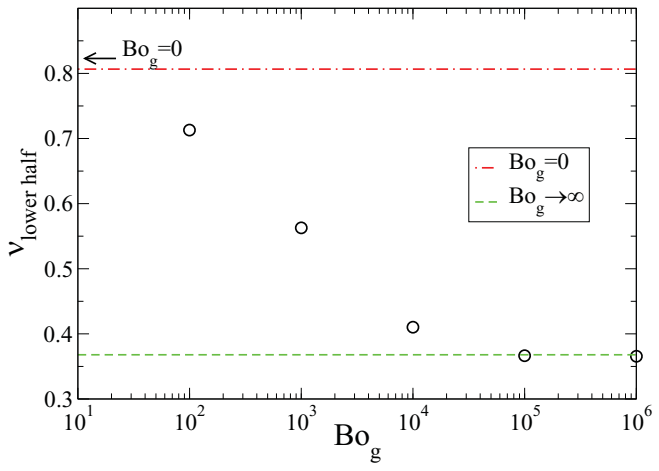

FIG. 3. (Color online) Average volume fraction $\nu_{\text{lower half}}$ depending on granular Bond number Bo_g. The density is averaged in the lower half of the system excluding the region very close to the bottom to avoid border effects. (Here we excluded the region below the height of 50 particle radii so that boundary effects are clearly removed for all curves; cf. Fig. 2.) Volume fractions vary between the two limits given by random close packing ($\mathrm{Bo}_g = 0$) and pure ballistic deposition ($\mathrm{Bo}_g \to \infty$).

number is plotted on a logarithmic scale; that is, to see substantial changes of volume fraction the cohesive force or the gravitational force has to be changed by orders of magnitude. Particles with similar gravity and cohesive force will show the same typical behavior. As typically both forces depend on the size of the particles, it appears to be natural to characterize the behavior of granular matter and powders by the grain size. For noncohesive material recent experimental, numerical, and theoretical studies [49–52] have investigated the influence of the friction coefficient on, for example, the volume fraction. A behavior similar to that found here for the cohesive material when varying the granular bond number has been found [49,50]: varying the friction coefficient on a logarithmic scale leads to a variation between the value 0.84 for the packing fraction of a random close packing and the value 0.77 for an infinitely large friction coefficient (in two dimensions or in three dimensions between 0.64 and 0.55). In the cohesive case as discussed here this range of accessible volume fractions is much higher and limited by the preparation protocol, that is, in this paper, by the ballistic deposition. This limit, of course, can be changed when changing the preparation protocol, for example, by introducing a capture radius (cf. Sec. VI).

For all results presented above the total system height H was fixed, that is, the deposition process stops when no more particles can be deposited below a specified value H. When comparing density profiles for different system heights, H plots depending on the vertical position y will show different densities. Scaling can be achieved when plotting the density versus the depth $H - y$ as illustrated in Fig. 4. This means that the upper part of the large system is depositing and collapsing in the same way as the small system while additionally leading to further collapse of the structure deposited previously below, accompanied by a downward motion of the whole upper part. Obviously the slow deposition process guarantees that inertia is not important (cf. Sec. VI).

The specific behavior of the density profiles shown in this section results from a deposition process combined with a

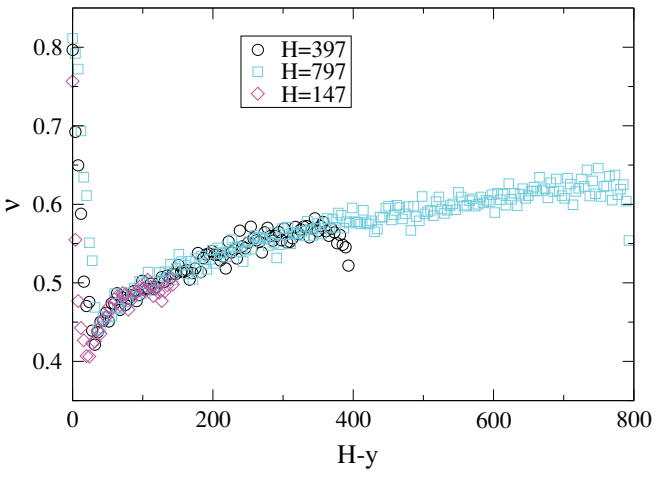

FIG. 4. (Color online) Illustration of the effect of system size for the intermediate density range (Bond number $\mathrm{Bo}_g = 10^3$). Plotting the depth $H - y$ measured from the surface H of the final packings, smaller systems show the same profile as large systems.

collapse of the current structure due to gravity. The deposition is characterized by the number of deposited particles per volume, which we call "deposition density" and which is not constant here (Sec. V). The collapse happens successively in relatively small avalanches, which are analyzed in detail in the following section. In Sec. V we show that these avalanches can be used to relate the final density profile to the "deposition density."

IV. ANALYSIS OF THE AVALANCHES DURING DEPOSITION AND COLLAPSE

Typically the collapsing of the structures, as mentioned earlier, happens discontinuously in small avalanches. As these avalanches are important also for the final density profiles (see Sec. III), their characteristics are studied in detail in this section. To illustrate the nature of these avalanches, in Fig. 5 the trajectories of the particles are plotted for a relatively small system of height $H = 147$ consisting of about 3200 particles (for better visibility only each fifth trajectory is shown, that is, the trajectories of 640 particles, instead of all 3200 particles). The avalanches are a collective motion of parts of the system. This mainly downward motion is accompanied by a sideward motion or rotation.

Upon zooming in, individual trajectories can be identified. These trajectories represent the motion of each particle during deposition and collapse. Thus, they show the paths that a particle experiences in all avalanches at different times. Neighboring particles can have very similar trajectories, that is, they belong to the same set of avalanches at different times.

In Fig. 6 we show the size of avalanches depending on the initial and final vertical position. This size is measured by Δy, the total downward displacement of the particle after its deposition, that is, initial position minus final position. This represents for each particle the sum of all avalanches occurring during the generation process, resulting in as many data points as particles in the system. In Fig. 6 these data are averaged in bins two particle diameters in size. The fluctuations within

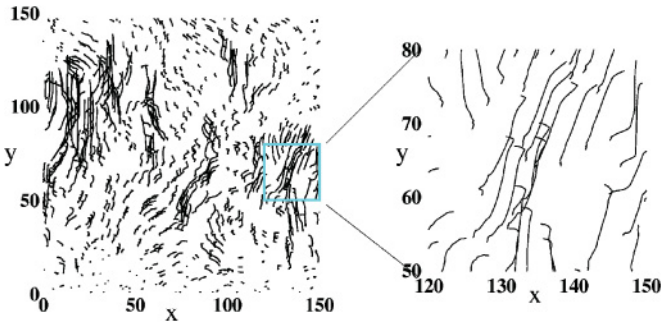

FIG. 5. (Color online) Particle trajectories of particles of a small system ($H = 147$; cf. Fig. 4) for the whole deposition and collapse. For better visibility only each fifth particle's trajectory is shown, that is, the trajectories of 640 particles (instead of all 3200 particles).Viewing the total system (and, at the right, a zoom-in of the boxed area on the left) illustrates that parts of the system move collectively downward, accompanied by a sideward motion or rotation. In the zoom-in at the right, individual trajectories can be identified, which are composed of the sum of paths during all the small avalanches experienced by the particle.

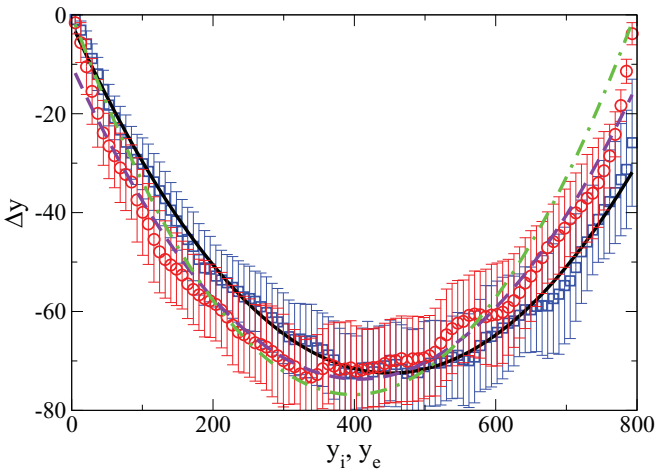

FIG. 6. (Color online) Size of avalanches depending on vertical position for $\mathrm{Bo}_g = 10^3$. Here the size is measured by Δy, the average total downward motion of a particle after deposition (initial position minus final position). On the horizontal axis the initial position y_i [(blue) squares] and final position y_e [(red) circles] are plotted. This leads to two slightly shifted curves as $y_e < y_i$. Solid lines represent parabolic fits $\Delta y(y_i) = -1.8 - 0.31 y_i + 0.000\,35 y_i^2$ [solid (black) line] and $\Delta y(y_e) = -10.2 - 0.31 y_e + 0.000\,38 y_e^2$ [dashed (violet) line]. Also shown is a fit by $\Delta y(y_e) = -a y_e (1 - y_e/H)$ predicted by the considerations in Sec. VII, leading to $a \approx 0.39$ [dashed-dotted (green) line].

each bin are shown by the vertical error bars. Both curves (for y_i and y_e) can be relatively well approximated by parabolas:

$$\Delta y(y_i) = a' + b' y_i + c' y_i^2, \quad \Delta y(y_e) = a + b y_e + c y_e^2 \qquad (1)$$

It is obvious that both curves cannot obey the parabolic behavior exactly, as y_i and y_e are related by $y_e(y_i) = y_i + \Delta y(y_i)$. However, in the cases presented in this section, obtained by slow deposition, the value of Δy is relatively small compared to y_i, so that $y_e(y_i)$ is very close to a straight line, leading only to a very small horizontal shift. This behavior is typical for intermediate Bond numbers, whereas in limiting cases no noticeable dependence of Δy on the vertical position could be found. For $\mathrm{Bo}_g = 0$ a small constant value, below the particle diameter (about 1.5 particle radii), is observed. In the case $\mathrm{Bo}_g \to \infty$ no collapse happens, that is, all $\Delta y = 0$.

The parabolic behavior can be reproduced also for other system heights. In Fig. 7 two different system sizes, again for $\mathrm{Bo}_g = 10^3$, are shown collapsed by scaling both axes by the system height H. From this scaling one can deduce the system size dependence of the prefactor of the quadratic term in Eq. (1). The scaling becomes

$$\Delta y(y, H) = H f(y/H) \propto H (y/H)^2 \propto 1/H \qquad (2)$$

when assuming that $\Delta y \propto y^2$ [parabolic behavior; see Eq. (1)]. This $1/H$ dependence could be verified by fitting the curves in Fig. 7. Note that the parabolic shape was also found when varying the friction coefficient μ and the rolling friction coefficient μ_r.

Whereas the average of the avalanche size Δy as a function of the vertical position shows a parabolic profile of reasonable quality, there are of course large fluctuations around this value. In Fig. 8 we show the distribution of the avalanche sizes (here

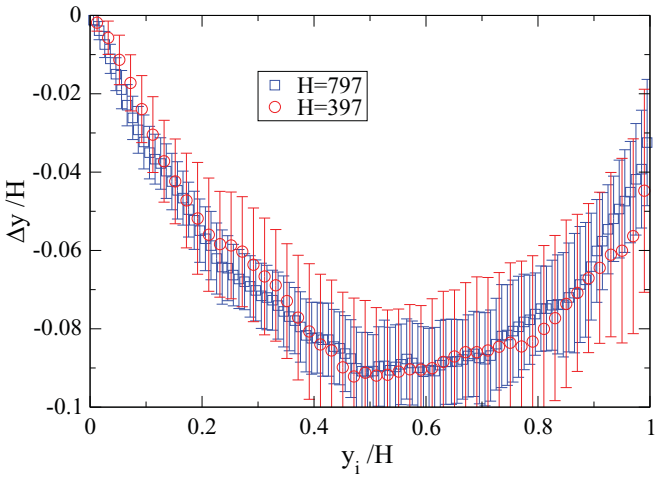

FIG. 7. (Color online) Collapse of the size of the avalanches for two different system sizes can be obtained by scaling both axes by the system height (here, $\mathrm{Bo}_g = 10^3$). Under the assumption of a parabolic profile this scaling leads to a $1/L$ dependence of c [prefactor of the quadratic term in Eq. (1)].

$|\Delta y|$) for the entire system, that is, independent of the vertical position. Upon removing the upper and lower part of the system to decrease boundary effects, we obtain a Gaussian distribution; that is, we get an estimate of a typical avalanche size. This typical size decreases with increasing Bond number, and in the limit of $\mathrm{Bo}_g \to \infty$, where no avalanches occur, it vanishes. In the limit of $\mathrm{Bo}_g = 0$ (no cohesion) the behavior is different, and an exponential decay is obtained (Fig. 9). Here the boundaries have no effect; that is, we get the same behavior when removing the upper and lower part of the system as done previously. For this Bond number typically the surface of the structure during deposition grows relatively flat, so that large $|\Delta y|$ are unlikely, as expressed by the exponential decay. Due to the monodispersity this surface is locally almost a flat crystalline surface with heaps that consist of only a few particles, in most cases one particle. When a particle is

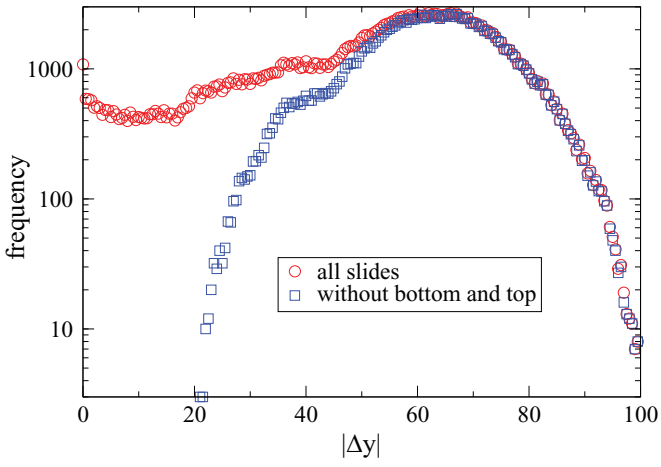

FIG. 8. (Color online) The histogram of the size of avalanches $|\Delta y|$ for $\mathrm{Bo}_g = 10^3$ basically follows a Gaussian. Deviation from this behavior can be almost fully suppressed when removing the bottom and top part of the system.

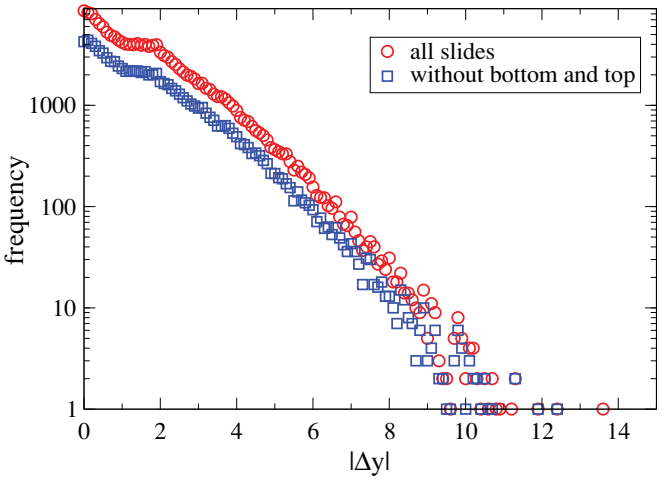

FIG. 9. (Color online) The histogram of avalanches $|\Delta y|$ for $\mathrm{Bo}_g = 0$ basically shows an exponential decay. Deviation from this behavior can be found for $|\Delta y|$ between 1 and 2 particle radii, where the probability is about constant. This effect cannot be suppressed when removing the bottom and top part of the system (as, e.g., for $\mathrm{Bo}_g = 10^3$).

deposited on a one-particle heap it rolls off to rest eventually as a "crystalline" neighbor beside the particle, resulting in a $|\Delta y|$ between 1 and 2. This leads to the very small range of $|\Delta y|$ with constant probability in Fig. 9. Taking a slightly polydisperse system, this region would disappear.

In this section we have studied the collapse of the structures occurring in small avalanches that we analyzed statistically. We suggest characterizing these avalanches by their "size" and their showing a typical dependence on vertical position and a parabolic shape for the specific systems investigated in this section. In the following section we use this characteristic behavior to derive the final density profile from the "deposition density." In Sec. VI the same concept is shown to be applicable also to other protocols of generating loose structures.

V. THEORETICAL ANALYSIS OF THE AVALANCHES

In previous sections we mentioned that the dynamics leading to the final configuration is determined by small avalanches occurring during the deposition process. All these compaction events are contained in the function $\Delta y(y_e)$, which is given by the difference between the initial position y_i and final position y_e. Note that Δy can be plotted (e.g., Fig. 6) as a function of the final position y_e or, alternatively, as a function of the position of deposition y_i. The aim of this section is to relate the final density profile to the dynamic process of deposition and collapse by using $\Delta y(y_e)$, showing how the avalanches produce the final density $\rho_f(y_e)$ from the deposition density $\rho_d(y_i)$. The deposition density is defined by the number of particles deposited within a volume. As the structure collapses between the depositions the deposition density is not independent of the collapsing, and it is possible that at (almost) the same position several particles are deposited. Thus, locally within a fixed volume even more particles could be deposited than is typical for a dense packing.

We first calculate the number $N_{d,f}$ of particles up to a given height $y_{i,e}$ (L_x width of the two-dimensional system in units of particle radii):

$$N_{d,f}(y_{i,e}) = L_x \int_0^{y_{i,e}} dy' \rho_{d,f}(y'). \tag{3}$$

The final position y_e of particles can be related to the position y_i of deposition by the avalanche profile Δy:

$$y_i(y_e) = y_e - \Delta y(y_e) \quad \text{or} \quad y_e(y_i) = y_i + \Delta y(y_i). \tag{4}$$

In this notation Δy is negative as the motion of the particles is downward (due to gravity). Therefore, y_i is larger than or equal to y_e. As particles are never destroyed, the number of particles deposited up to a given height $N_d(y_i)$ will stay the same, but shifted to a lower height, $N_f(y_e)$, where y_i and y_e are related by Eq. (4). Together with Eq. (3) this leads to

$$N_f(y_e)/L_x = N_d(y_i(y_e))/L_x = \underbrace{\int_0^{y_i(y_e)} dy' \rho_d(y')}_{\equiv G(y_i(y_e))}. \tag{5}$$

This relates N_f to the deposition density, whereas Eq. (3) relates N_f to the final density. The function G here is formally introduced as an abbreviation for the integral; by derivation of G the density is retrieved. The final density can be obtained by derivation of N_f/L_x using Eq. (5):

$$\begin{aligned}\rho_f(y_e) &= \frac{d}{dy_e}\frac{N_f(y_e)}{L_x} = \frac{d}{dy_e}G(y_i(y_e)) = \frac{dG(y_i)}{dy_i}\frac{dy_i}{dy_e} \\ &= \rho_d(y_i(y_e))\frac{dy_i}{dy_e} \\ &= \rho_d(y_i(y_e))\left(1 - \frac{d\Delta y(y_e)}{dy_e}\right). \end{aligned} \tag{6}$$

The deposition density $\rho_d[y_i(y_e)]$, in principle, can be expressed directly by y_e upon introducing $\rho'_d(y_e)$. As usual, the functional behavior of either function is not known, but only values for specific y_i and y_e; the transformation can be done for each point by simply using Eq. (4), that is, replacing each y_i by $y_e = y_i + \Delta y(y_i)$. Summarizing, to calculate the final density profile one needs to know the deposition density ρ_d and the avalanche profile Δy. Note that the avalanche profile dependence on both y_e and y_i is needed, which can be calculated from each other for some cases as shown later. For experimental situations these quantities are not known. However, the relation between ρ_f and ρ_d [Eq. (6)] can be used to calculate the deposition density from the final density in the slow deposition limit, when assuming a parabolic profile as found in the simulations before.

In Fig. 10 we use Eq. (6) to calculate the final density from the deposition density by using the parabolic fit for Δy (Fig. 6). In practice, first the deposition density curve is shifted on the horizontal axis by $y_e = y_i - (a' + b' y_i + c' y_i^2)$, then the deposition density is multiplied by the factor on the right of Eq. (6), using the derivative of $\Delta y(y_e)$, given by Eq. (1), leading to $1 - (b + 2cy_e)$ which is a linear function. If the deposition density were constant, this would lead to a linear profile for the final density. However, the deposition density is not constant, explaining the nonlinear behavior for the final density. Additionally, the deposition density shows strong

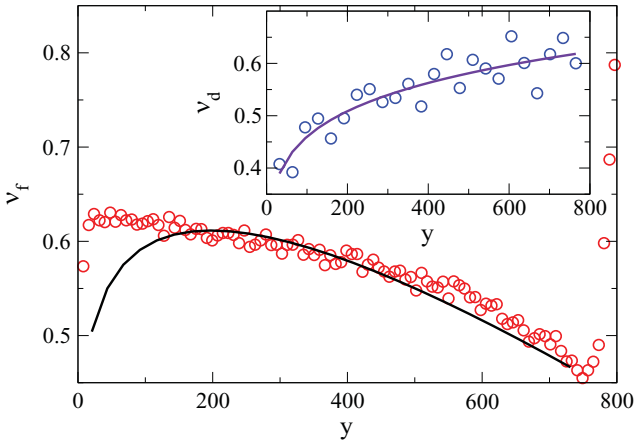

FIG. 10. (Color online) Using the parabolic approximation (Fig. 6) for the average avalanches, the final density (here, the volume fraction ν_f) can be calculated from the deposition density (inset: volume fraction ν_d for $\mathrm{Bo}_g = 10^3$). There are strong fluctuations in the deposition density, which are induced by the irregularity of the avalanches. To obtain a smooth curve we use a fit function (here, the power-law fit, with exponent 0.15) to calculate a final density [solid (black) line] that matches relatively well with the measured density profile for sufficiently large y (except close to the bottom).

fluctuations, but by assuming the avalanches to follow the averaged parabolic behavior, the corresponding fluctuations in the avalanche profile are not included. The calculated curve matches relatively well the profile measured in the simulations for sufficiently large values of the vertical position. Close to the bottom, however, the calculated curve deviates from the measured one. In this region the deposition density is very low, that is, almost that of pure ballistic deposition. This can be understood, as the system needs to gain a sufficient amount of weight for the collapse to start (cf. also Sec. VI). This should correspond to a higher initial slope of $\Delta y(y_e)$, which is not reflected in the parabolic approximation [Eq. (1)]. In this region higher-order terms would be necessary to reproduce the system bottom also.

The same analysis has been done also, for example, for $\mathrm{Bo}_g = 10^2$, as shown in Figs. 11 and 12. In this case the deposition density shows somewhat lower fluctuations as for $\mathrm{Bo}_g = 10^3$ (Fig. 10). To quantify this we estimated the fluctuations of the deposition density at vertical position $y = 200$ for both cases. For $\mathrm{Bo}_g = 10^2$ we obtained about 15%, whereas we estimated about 20% for $\mathrm{Bo}_g = 10^3$. For the case of $\mathrm{Bo}_g \to \infty$ there is no avalanching at all (cf. Sec. IV), and trivially the final density equals the deposition density. This is very similar for very large Bo_g, but as some avalanches occur there are some relatively small fluctuations in the average profile. Away from this limit, but still close enough that the density profile is very similar to the $\mathrm{Bo}_g \to \infty$ case, as, for example, for $\mathrm{Bo}_g = 10^4$, very large fluctuations in the avalanche profile are observed. Thus, the parabolic profile cannot easily be identified. Still the theory works well, as the final density is very close to the deposition density, so that even a very inaccurate fit for the avalanche profile does not affect the calculated density profile very much. In the limit of $\mathrm{Bo}_g = 0$ the avalanche profile is a constant (cf. Sec. IV); that is, all grains are slightly shifted downward by the same amount

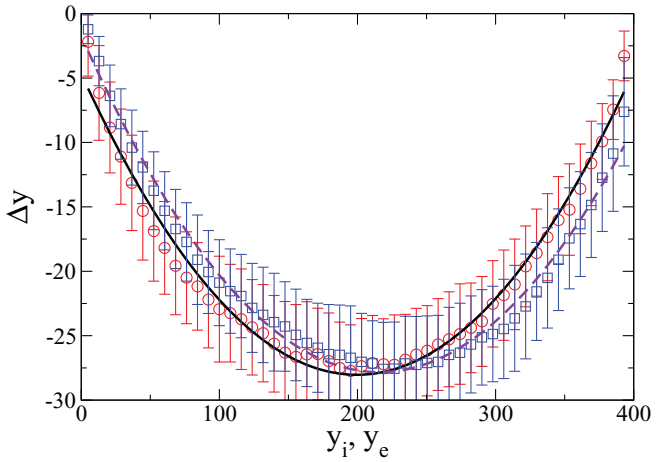

FIG. 11. (Color online) Size of avalanches depending on vertical position for $\mathrm{Bo}_g = 10^2$. Here the size is measured by Δy, the total downward motion of the particle after deposition (initial position minus final position). On the horizontal axis the initial position y_i [(blue) squares] and final position y_e [(red) circles] are plotted. Lines represent the parabolic fits $\Delta y(y_i) = -1.7 - 0.24 y_i + 0.00056 y_i^2$ [dashed (violet) line] and $\Delta y(y_e) = -4.7 - 0.23 y_e + 0.00059 y_e^2$ [solid (black) line].

(except boundary effect at the bottom). As the derivative then vanishes, the final density equals the deposition density.

Here, we have shown how the parabolic avalanche profile can be used to calculate the final density profiles from the deposition density in the case where gravity acts during deposition. In the next section the same concept is used in the simpler case of collapse of the system after deposition is complete. These two cases are then related in Sec. VII.

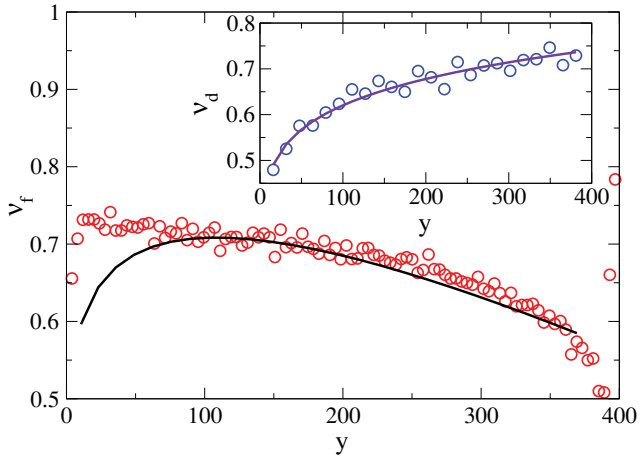

FIG. 12. (Color online) Using the parabolic approximation (Fig. 11) for the average avalanches the final density can be calculated from the deposition density (here, volume fraction for $\mathrm{Bo}_g = 10^2$). There are strong fluctuations in the deposition density, which are induced by the irregularity of the avalanches. As before (for $\mathrm{Bo}_g = 10^3$), to obtain a smooth curve we use a fit function (here, the power-law fit, with exponent 0.13) to calculate a final density [solid (black) line] that matches relatively well for sufficiently large y (except close to the bottom).

VI. COLLAPSE AFTER DEPOSITION IS COMPLETE

In the previous sections we have investigated the case where gravity acts during deposition, leading to a relatively complex shape of the density profiles and parabolic characteristics of the avalanche size. For this case we have shown that these avalanche profiles can be used to relate the final density profile to the deposition density. In this section we analyze the case when the particles are first deposited, then gravity is switched on and the structures collapse. This case is even simpler and can later be used to understand the more complex system studied before. In this case the initial density ρ_i characterizes the system (instead of the deposition density as in the previously discussed situation). Using the off-lattice version of ballistic deposition as presented in Refs. [41] and [42] with sticking probability 1, vertically falling particles stick when they touch an already deposited particle. This leads to a fixed initial density. Lower densities can be obtained by using a capture radius r_{capt}; that is, particles stick to each other when they are within a certain distance during the falling of the depositing particle. More precisely, when the distance between the centers of mass of two particles is below $2 \cdot r_{\mathrm{capt}}$, the particles stick and the falling particle is pulled along the connecting line toward the already deposited particle. This capture radius is a measure for the distance between the branches of the deposit and the resulting density is inversely proportional to r_{capt} [32]; $r_{\mathrm{capt}} = 1$ gives the original method. The resulting initial structures are shown in Fig. 13. These structures, obtained with different capture radii, are used later to study the influence of the initial density.

First, we investigate the behavior using $r_{\mathrm{capt}} = 1$. Figure 14 shows the density profile before the collapse, which is the same that we got in the limit of $\mathrm{Bo}_g \to \infty$ in Sec. III, also independent of vertical position. After this deposition is complete, gravity is "switched on" and the structure abruptly collapses. Here we choose a Bond number of $\mathrm{Bo}_g = 10^3$. This leads to a final structure with a higher density, in this case also independent of the vertical position (Fig. 14). As no particles are added after the initial deposition, the final system height is lower.

Similarly as before, we analyze the size of the avalanches Δy as defined in Sec. IV. Figure 15 shows a linear dependence of Δy on both y_e and y_i. The fit parameters of the two lines can be related to each other by the relation between y_i and y_e [Eq. (4)]. Assuming $\Delta y(y_e) = a - b y_e$ and $\Delta y(y_i) = a' - b' y_i$, the values a' and b' can be calculated from a and b (see Appendix A) as

$$b' = \frac{b}{1+b}, \qquad a' = \frac{a}{1+b}. \tag{7}$$

The vertical dependence of Δy can be used similarly as before to calculate the final density from the initial density by using Eq. (6). The calculated density profile using this linear dependence reproduces the obtained final density profile very well, as shown in Fig. 14. In this case the agreement is better, as now the initial density is not fluctuating very much, in contrast to the cases discussed in Sec. V. The density increase $\Delta\rho$ (or volume fraction increase $\Delta\nu$) can be directly calculated by the

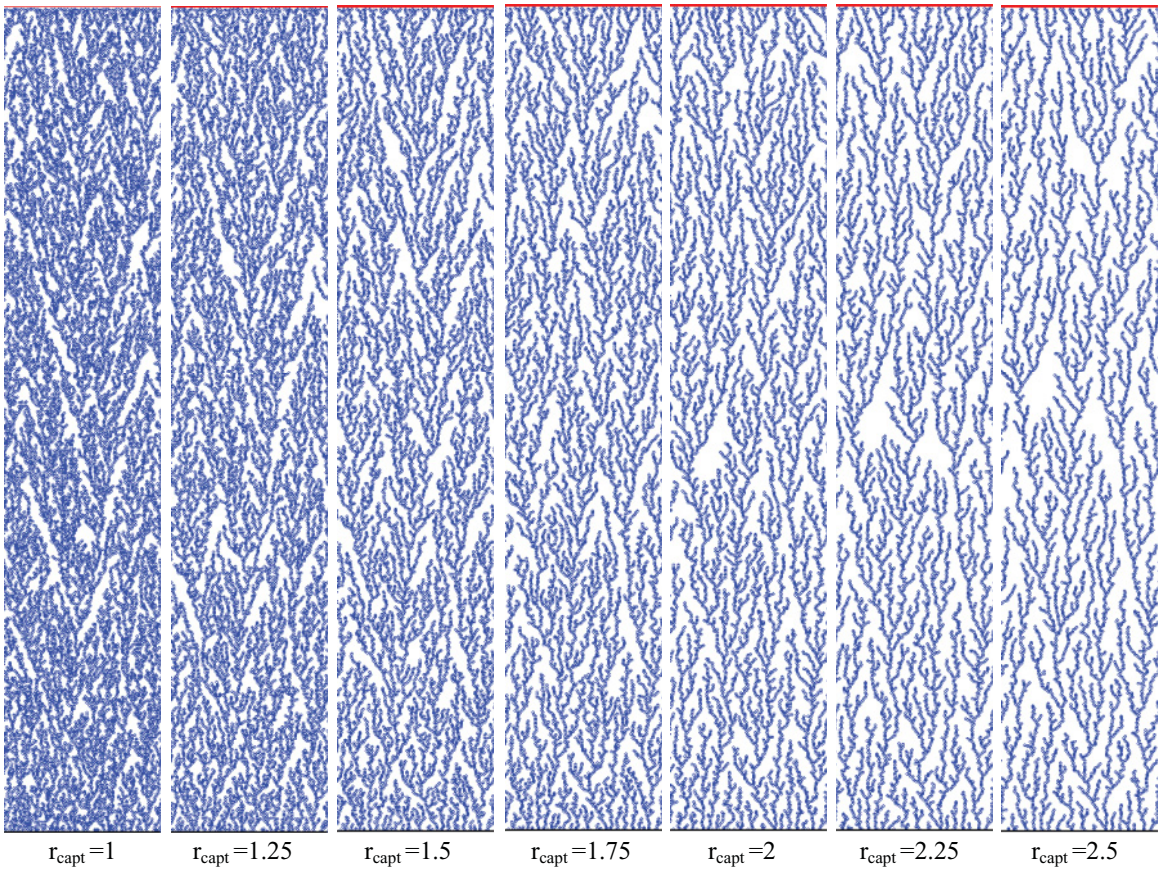

FIG. 13. (Color online) Initial structures generated by ballistic deposition with increasing capture radius r_{capt}.

constant slope of $\Delta y(y_e)$:

$$\frac{\Delta\rho}{\rho_i} = \frac{\Delta v}{v_i} = -\frac{d\Delta y(y_e)}{dy_e}. \tag{8}$$

For the same parameters ($\text{Bo}_g = 10^3$) we studied the effect of the system height H on the density increase while still keeping the initial density fixed (Fig. 16). A logarithmic fit matches the data best. This fit certainly cannot continue to infinity, as there is a limit for the density $\rho_{\max}$ given by the random close packing (see also Fig. 3), leading to a $(\Delta v/v_i)_{\max}$ of 1.19 ($\simeq \rho_{\max}/\rho_{\text{ini}} - 1$).

Using initial capture radii as described above we study the influence of the initial density on the relative density increase $\Delta v/v_i$ (Fig. 17). We obtain the best fit when using a power law with an exponent ofabout 1.64.

We have shown in this section that the linear avalanche profile is a characteristic feature of compacting from a structure

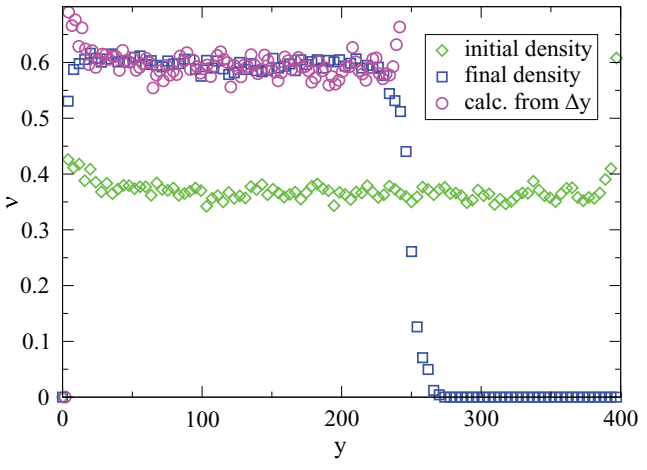

FIG. 14. (Color online) The initial and final density are almost constant when first depositing and then collapsing the system ($\text{Bo}_g = 10^3$). Using the linear dependence of the avalanches Δy on the vertical position (see Fig. 15), the final density can be calculated from the initial density using Eqs. (4) and (6). Results support the analytical considerations.

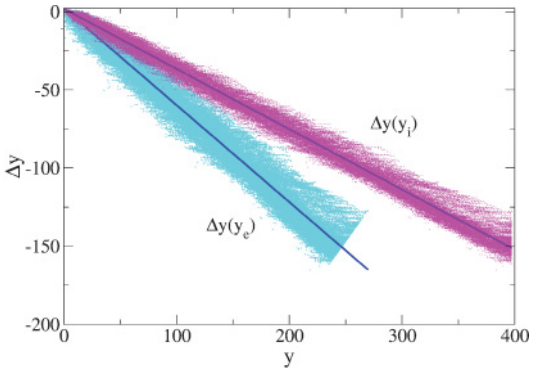

FIG. 15. (Color online) The linear dependence of the avalanche sizes $\Delta y(y_{i,e})$ explains the homogeneous density increase shown in Fig. 14. Linear fits are $\Delta y(y_e) = 2.2 - 0.62 y_e$ and $\Delta y(y_i) = 1.9 - 0.39 y_i$.

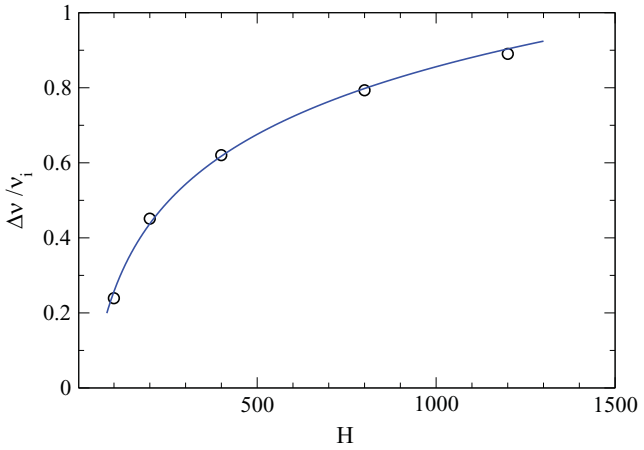

FIG. 16. (Color online) Dependence of volume fraction increase $\Delta v/v_i$ on system height H when the system is first deposited and then collapsed. A logarithmic fit matches the data best [here $y = -0.94 + 0.26\ln(x)$]. The limit of random close packing defines the largest possible value for $\Delta v/v_i$ of 1.19, which will be approached for infinite system heights.

with depth-independent density to a structure with again depth-independent density, obtained here for systems generated by ballistic deposition collapsing due to gravity. More complex avalanche profiles with nonconstant derivatives will transform homogeneous structures into inhomogeneous structures. Thus, we expect the linear profile to be obtained in all cases where a homogeneous initial system compacts to a homogeneous final system. These homogeneous compaction processes are investigated in different research areas, as discussed, for example, in Refs. [53–57]. In addition, in the next section we show that also for the more complex process when gravity acts during deposition (Sec. III), this linear profile can be used to derive the parabolic profile of the avalanches.

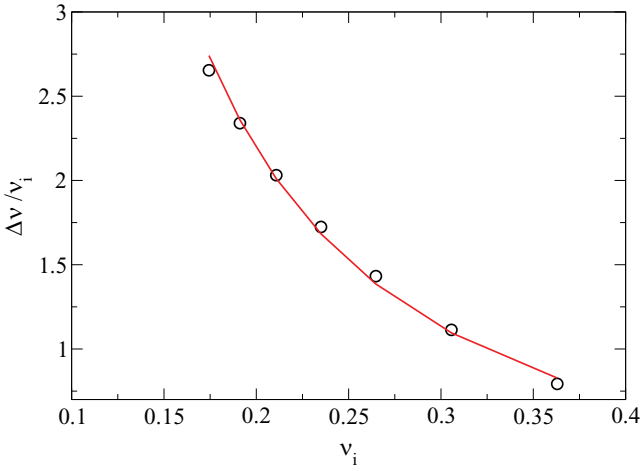

FIG. 17. (Color online) Dependence of volume fraction increase $\Delta v/v_i$ on volume fraction v_i of the initial system (system first deposited and then collapsed). Different densities were reached by increasing the capture radius for ballistic deposition (Fig. 13). A power-law fit with exponent 1.64 fits relatively well (power-law fit results in $y = 0.158x^{-1.64}$).

VII. RELATION BETWEEN DEPOSITION UNDER GRAVITY AND SWITCHING ON GRAVITY AFTER DEPOSITION

For the very fast process a linear profile for Δy depending on vertical position has been found (cf. Fig. 15), whereas the slow deposition limit shows a parabolic profile for Δy depending on vertical position (cf. Figs. 6 and 11). In this section we discuss how a relation between both can be established. By this relation also the parabolic profile is put into a more fundamental basis like the linear profile for the homogeneous collapse.

Let us imagine depositing particles slice by slice as sketched in Fig. 18. The slices are thin parts of the system in the vertical direction spanning the full system width in the horizontal direction. They can be considered as systems with a very small initial height h_0. In each slice the deposition will be immediately followed by the collapse. However, there will be not only an "internal collapse" within the "freshly" deposited slice, but also a compaction of the slices below, due to the additional weight of the "freshly" deposited slice.

Let us first consider systems composed of a small number n of slices. The case $n = 1$ (one slice) is the same as discussed in the previous section: the system collapses "internally," leading

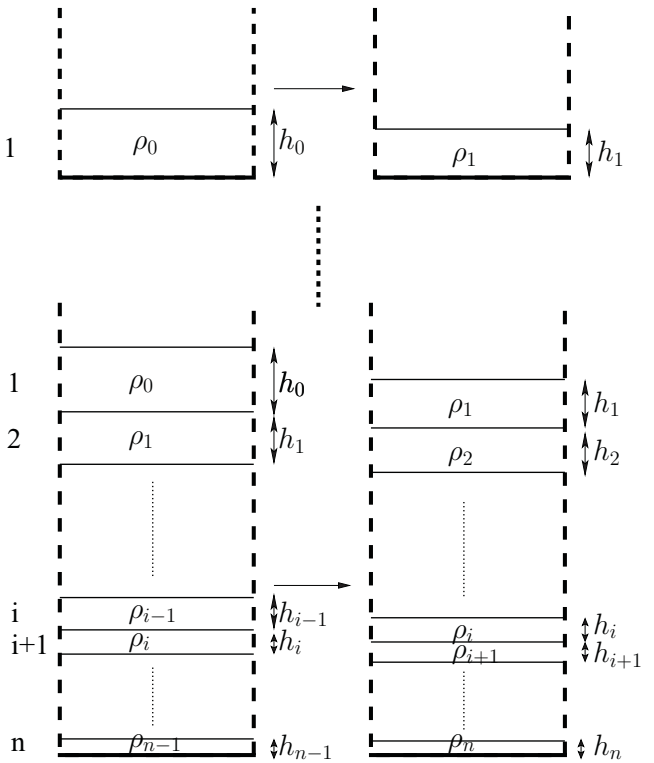

FIG. 18. Sketch illustrating the procedure of depositing the grains slice by slice. The first slice deposited is compacted by internal collapse. The same is true for each "freshly" deposited slice. The slices below are compacted by the added weight of the slices above. Periodic boundary conditions in the horizontal direction are imposed (dashed lines). The figure also illustrates the definition of the symbols used here. The n slices are numbered from 1 to n. A slice i collapses from ρ_{i-1} to ρ_i while its height decreases from h_{i-1} to h_i, where $h_i = \rho_{i-1}/\rho_i h_{i-1}$.

to an increase in the density from ρ_0 to ρ_1, while the height decreases from h_0 to h_1. Here we denote the slice number as 1 (cf. Fig. 18). As shown in the previous section the avalanche sizes have a linear profile $\Delta y(y_e^{(1)}) = S_1 y_e^{(1)}$. S_1 is the slope in slice 1 and is the same for all freshly deposited slices when the height h_0 is kept constant. The vertical position $y_e^{(1)}$ within slice 1 is measured from its bottom ($y_e^{(1)} = 0, \ldots, h_1$). This notation is used in the following for each slice i: $y_e^{(i)} = 0, \ldots, h_i$. The case $n = 2$ (two slices) means adding an additional slice to the case $n = 1$. Then the lower slice (slice 2) experiences an additional compaction by the added weight expressed by the corresponding avalanche size $C_2 y_e^{(2)}$ assuming a linear behavior for this relatively fast process, similar to that for the internal collapse. This is justified at least for the limit of small slices considered later in this section. The upper slice (slice 1) will be compacted internally and, additionally, will move downward by $C_2 h_2$ ($= h_1 - h_2$), as the slice below is compacted. Summarizing for the two slices, we get

$$\begin{aligned} \Delta y^{(1)}\left(y_e^{(1)}\right) &= S_1 y_e^{(1)} + \underbrace{C_2 h_2}_{h_1 - h_2}, \\ \Delta y^{(2)}\left(y_e^{(2)}\right) &= C_2 y_e^{(2)} + S_1 \underbrace{(1 + C_2) y_e^{(2)}}_{y_e^{(1)}}. \end{aligned} \tag{9}$$

For slice 2 the internal compaction from the first step $S_1 y_e^{(1)}$ has been transformed by using that $\rho_2 = (1 + C_2)\rho_1$ [cf. Eq. (8)], leading to $h_2 = \rho_1/\rho_2 h_1 = 1/(1 + C_2)h_1$. Adding a further slice leads to the case $n = 3$, where the two slices are compacted due to the additional weight. Each of these compactions is accompanied by a downward shift of the slices above. This leads to

$$\begin{aligned} \Delta y^{(1)}\left(y_e^{(1)}\right) &= S_1 y_e^{(1)} + \underbrace{C_2 h_2 + C_3 h_3}_{(h_1 - h_2) + (h_2 - h_3) = h_1 - h_3}, \\ \Delta y^{(2)}\left(y_e^{(2)}\right) &= C_2 y_e^{(2)} + \underbrace{S_1(1 + C_2) y_e^{(2)} + C_2 h_2}_{\text{from step 2}} + C_3 h_3, \\ \Delta y^{(3)}\left(y_e^{(3)}\right) &= C_3 y_e^{(3)} \\ &\quad + \underbrace{C_2(1 + C_3) y_e^{(3)} + S_1(1 + C_2)(1 + C_3) y_e^{(3)}}_{\text{from step 2}}. \end{aligned} \tag{10}$$

Imagining continuing this iterative procedure, one obtains the case of n slices. For the top slice this results in

$$\Delta y^{(1)}\left(y_e^{(1)}\right) = S_1 y_e^{(1)} + \underbrace{C_2 h_2 + C_3 h_3 + \cdots + C_n h_n}_{h_1 - h_n}. \tag{11}$$

The first term is the internal collapse, whereas the other terms are the shift due to the compaction of all slices below (2 to n) in this last step. For the bottom slice we get

$$\begin{aligned} \Delta y^{(n)}\left(y_e^{(n)}\right) &= S_1(1 + C_2)(1 + C_3) \times \cdots \times (1 + C_n) y_e^{(n)} \\ &\quad \times C_n y_e^{(n)} + C_{n-1}(1 + C_n) y_e^{(n)} + \cdots + C_2 \\ &\quad \times (1 + C_n)(1 + C_{n-1}) \times \cdots \times (1 + C_3) y_e^{(n)}. \end{aligned} \tag{12}$$

Here all terms represent a collapse in the slice either internally, by its own weight, when deposited in the first step or when collapsing due to added weight in the following steps. In addition, these collapses have to be transformed to a $y_e^{(n)}$ dependence (see above). For an arbitrary slice i somewhere in the system we get both types of terms as in Eqs. (11) and (12):

$$\begin{aligned} \Delta y^{(i)}\left(y_e^{(i)}\right) &= S_1(1 + C_2) \times \cdots \times (1 + C_i) y_e^{(i)} \\ &\quad \times C_i y_e^{(i)} + C_{i-1}(1 + C_i) y_e^{(i)} \\ &\quad + \cdots + C_2(1 + C_3) \times \cdots \times (1 + C_i) y_e^{(i)} \\ &\quad \underbrace{+ C_n h_n + C_{n-1} h_{n-1} + \cdots + C_{n-i+1} h_{n-i+1}}_{h_{n-i} - h_n} \\ &\quad \underbrace{+ C_{n-1} h_{n-1} + \cdots + C_{n-i} h_{n-i}}_{h_{n-i-1} - h_n} \\ &\quad \vdots \\ &\quad \underbrace{+ C_{i+1} h_{i+1} + \ddots + C_2 h_2}_{h_1 - h_{i+1}}. \end{aligned} \tag{13}$$

The part of the expression independent of $y_e^{(i)}$ represents the shift due to compaction by the weight of the slices added above in $n - i$ steps considering all slices below. It consists of $n - i$ times $i - 1$ terms and can be written shortly as

$$\Delta y_{\text{shift}}^{(i)} = \sum_{j=1}^{n-i} h_j - h_{j+i}. \tag{14}$$

The limit of large n while keeping the total system height constant gives very small slices where the part $\Delta y_{\text{shift}}^{(i)}$ dominates, as for very small systems the internal collapse almost vanishes (cf. Fig. 16). Therefore, in the following we only consider this term to show that we obtain an approximately parabolic behavior. Let us assume that the h_i are linear in i:

$$h_i = \left(1 - a\frac{i}{n}\right) h_0, \quad a < 1. \tag{15}$$

This means that deeper in the system (larger i), the width of the slice is smaller. Note that for the case $a \ll 1$ this can be understood as a linearization. This case means that the overall compaction is not large as it is in the case for intermediate Bond numbers. From Eqs. (14) and (15) we obtain

$$\begin{aligned} \Delta y_{\text{shift}}^{(i)} &= \sum_{j=1}^{n-i} \left(1 - a\frac{j}{n}\right) h_0 - \left(1 - a\frac{j+i}{n}\right) h_0 \\ &= \sum_{j=1}^{n-i} a\frac{i}{n} h_0 = (n - i) a\frac{i}{n} h_0. \end{aligned} \tag{16}$$

This is a quadratic dependence on the slice number i. For comparison with our results we have to transform i to a vertical position y_e, which is obtained when summing up the height h_i of all slices:

$$y_e(i) = \sum_{j=n}^{i+1} h_j = \sum_{j=1}^{n-i} h_{j+i}. \tag{17}$$

Using approximation (15) we obtain

$$y_e(i) \simeq \sum_{j=1}^{n-i} \left(1 - a\frac{j+i}{n}\right) h_0 \tag{18}$$

$$= h_0 \left[n - \frac{a}{2}(n^2 - n)\right] - i h_0 [1 - a(n - 1/2)]. \tag{19}$$

The detailed derivation is given in Appendix B. From this equation we can obtain $i(y_e)$

$$i = \frac{-y_e}{h_0\,[1 - a(n - 1/2)]} + \frac{n - a/2(n^2 - n)}{1 - a(n - 1/2)}. \tag{20}$$

We assume that we are in the limit of relatively small a. Neglecting all terms in a in Eq. (20) corresponds to neglecting terms in a^2 in Eq. (16). With this simplification and additionally using $h_0 = H/n$, we obtain $i = n - y_e/h_0 = n(1 - y_e/H)$, leading to

$$\Delta y_{\text{shift}}(y_e(i)) = [n - i(y_e)] i(y_e) \frac{Ha}{n^2} \tag{21}$$

$$= a y_e \left(1 - \frac{y_e}{H}\right). \tag{22}$$

This behavior is plotted in Fig. 6 (green curve). Note that in this figure the Δy is negatively defined, as opposed to the definition used in this section. This curve fits the measured curves relatively well except coming close to the top. This can be explained by the existence of a small "crust," that is, an accumulation of particles at the top of the system in the simulations that is not considered in the analysis in this section. Probably this is also the reason for the slightly different prefactors of the parabola: from Eq. (22) we obtain $a = 0.39$, leading to a prefactor of the quadratic term of $a/H = 0.000\,49$, which is somewhat larger than the value of $0.000\,38$ obtained previously. The value of $a = 0.39$ is at least reasonably small, to ensure that the considerations of this section agree roughly with the simulation results. Previously by scaling Δy for different system sizes we obtained that the prefactor of the parabola scales as $1/H$ [cf. Eq. (2)]. This implies that a is independent fn system size H, for each specific Bond number, additionally indicating by its value how good the approximations in this section are.

Thus, in the limit of small a we could show that the linear behavior of Δy when collapsing after deposition is complete leads to a parabolic behavior when collapsing during deposition. Note that this a represents the difference in height of the top and the bottom slice; that is, the assumption of small a is true when the density difference between the density close to the bottom and that at the top is small, which is the case in all cases studied here (cf. Fig. 2). In the structures studied within our model in the previous sections (see, e.g., Sec. III), a small "crust" (particle accumulation) at the top again leads to a density increase. This will lead to a shift in the parabolic profile to the right (to the top). As discussed previously the deposition and collapse process is not continuous, so that the parabola is only an average of a very noisy distribution of Δy. Additionally, the deposition density is not constant, but slightly increasing (cf. Figs. 10 and 12), accompanied by relatively large fluctuations. For these reasons we can only expect a rough matching of our theory with the simulations. Nevertheless the parabolic behavior has been observed relatively clearly.

VIII. CONCLUSION AND OUTLOOK

We have studied the generation of fragile granular structures by a deposition and collapse process. In one extreme case where the deposition is sufficiently slow to allow the system to collapse and relax due to gravity after the deposition of each single grain, we studied the influence of the granular Bond number on the density profile. For intermediate Bond numbers the density decreases with height due to the compaction of the powder's own weight. We studied the generation process dynamics, which is discontinuous in small avalanches. These avalanches show a parabolic behavior and can be used to calculate the final density profile from the deposition density. In the other extreme case of collapse after deposition is complete, we found that the density is constant with vertical position and that the avalanche size depends linearly on the vertical position. We related the parabolic behavior to the linear one by imagining a slice-by-slice deposition and collapse process. Note that the linear behavior investigated here for the case of ballistic deposition followed by a gravitational collapse will be found for all collapse or compaction processes of homogeneous initial structures to homogeneous final structures. Therefore the concept of avalanches introduced in this paper is of general applicability to granular structures collapsing due to gravity or similar forces.

Our results may be directly verified experimentally, as already mentioned in Sec. I, for example, by using a Hele-Shaw cell [43–45], which can be tilted to effectively change gravity. To apply the model presented here more specifically, for example, for snow compaction, more realistic microscopic properties including aging processes would have to be used. For cake formation processes, instead of gravity, a porosity-dependent drag force could be applied. In this context an explicit consideration of the pore fluid or gas could be needed. The influence of the pore fluid or gas should be studied, in particular, for the fast compaction process presented in this paper.

ACKNOWLEDGMENTS

We thank Professor Dietrich Wolf for fruitful discussions and the DFG (Project No. HE 2732/11-1) for financial support.

APPENDIX A: RELATION BETWEEN SLOPES

The linear dependence of avalanches is found as well in y_e as in y_i (see Fig. 15). In this section the relation between the two lines is derived in detail. Assuming

$$\Delta y(y_e) = a - b y_e \quad \text{and} \quad \Delta y(y_i) = a' - b' y_i, \tag{A1}$$

the values a' and b' can be calculated from a and b as shown in the following. The relation between y_i and y_e can be

written as

$$y_i = y_e - \Delta y(y_e) = y_e - (a - by_e) \tag{A2}$$

$$= y_e(1+b) - a \tag{A3}$$

$$\Longrightarrow y_e = \frac{a}{1+b} + \overbrace{\frac{1}{1+b}}^{1+b-b} y_i \tag{A4}$$

$$= y_i\left(1 - \frac{b}{1+b}\right) + \frac{a}{1+b}. \tag{A5}$$

According to Eqs. (4) and (A1) y_e can be written as

$$y_e = y_i + (a' - b'y_i). \tag{A6}$$

Comparing Eqs. (A5) and (A6) results in

$$b' = \frac{b}{1+b}, \quad a' = \frac{a}{1+b}. \tag{A7}$$

From this or by a similar derivation the inverse relations can also be obtained:

$$b = \frac{b'}{1-b'}, \quad a = \frac{a'}{1-b'}. \tag{A8}$$

APPENDIX B: DERIVATION OF $y_e(i)$ IN LINEAR APPROXIMATION FOR h_i

Here we show the details of the derivation to obtain Eq. (19) from Eq. (18):

$$y_e(i) \simeq \sum_{j=1}^{n-i}\left(1 - a\frac{j+i}{n}\right)h_0$$

$$= h_0(n-i) - \frac{ha}{n}\left(\underbrace{\sum_{j=1}^{n-i} i}_{(n-i)i} + \underbrace{\sum_{j=1}^{n-i} j}_{(n-i+1)(n-i)/2}\right)$$

$$= h_0(n-i) - h_0 a(n-i)i/n - h_0 a(n-i-1)(n-i)/2$$

$$= h_0(n-i) - h_0 a\left[\frac{n}{2}(n+1) - i((n+1)/2 + n/2)\right]$$

$$= h_0\left[n - \frac{a}{2}(n^2-n)\right] - ih_0\left[1 - a(n-1/2)\right].$$

[1] J. Mitchell and K. Soga, *Fundamentals of Soil Behavior* (Wiley, Hoboken, NJ, 2005), 3rd ed.
[2] L. Barden, A. McGown, and K. Collins, Eng. Geol. **7**, 49 (1973).
[3] A. Assallay, C. Rogers, and I. Smalley, Eng. Geol. **48**, 101 (1997).
[4] Y. Reznik, Eng. Geol. **78**, 95 (2005).
[5] P. G. Rognon, J.-N. Roux, D. Wolf, M. Naaïm, and F. Chevoir, Europhys. Lett. **74**, 644 (2006).
[6] N. J. Wagner and J. F. Brady, Phys. Today **62**, 27 (2009).
[7] E. D. Gado and W. Kob, Soft Matter **6**, 1547 (2010).
[8] D. Kadau, H. Herrmann, J. Andrade Jr., A. Araújo, L. Bezerra, and L. Maia, Granular Matter **11**, 67 (2009).
[9] D. Kadau, H. Herrmann, and J. Andrade Jr., Eur. Phys. J. E **30**, 275 (2009).
[10] S. Manley, J. M. Skotheim, L. Mahadevan, and D. A. Weitz, Phys. Rev. Lett. **94**, 218302 (2005).
[11] Q. Wu, Y. Andreopoulos, S. Xanthos, and S. Weinbaum, J. Fluid Mech. **542**, 281 (2005).
[12] J. Heierli, J. Geophys. Res. [Earth Surface] **110**, F02008 (2005).
[13] D. Kadau, H. Herrmann, and J. Andrade Jr., in *Powders and Grains 2009, AIP Conference Proceedings, vol. 1145*, edited by M. Nakagawa and S. Luding (American Institute of Physics, Melville, NY, 2009), pp. 981–984.
[14] R. Bürger, F. Concha, and K. H. Karlsen, Chem. Eng. Sci. **56**, 4537 (2001).
[15] M. L. Aguiar and J. R. Coury, Ind. Eng. Chem. Res. **35**, 3673 (1996).
[16] K. Stamatakis and C. Tien, Chem. Eng. Sci. **46**, 1917 (1991).
[17] W.-M. Lu and K.-J. Hwang, AIChE **41**, 1443 (1995).
[18] C.-H. Ling, J. Glaciol. **31**, 194 (1985).
[19] T. U. Kaempfer and M. Schneebeli, J. Geophys. Res. **112**, D24101 (2007).
[20] R. Vetter, S. Sigg, H. Singer, D. Kadau, H. Herrmann, and M. Schneebeli, Europhys. Lett. **89**, 26001 (2010).
[21] D. B. Bahr, E. W. H. Hutton, J. P. M. Syvitsky, and L. F. Pratson, Comput. Geosci. **27**, 691 (2001).
[22] U. Bayer, Geol Rundschau **78**, 155 (2989).
[23] L. F. Athy, Bull. Am. Assoc. Petrol. Geol. **14**, 1 (1930).
[24] M. Roeck, M. Morgeneyer, J. Schwedes, L. Brendel, D. Wolf, and D. Kadau, Part. Sci. Technol. **26**, 43 (2008).
[25] M. Roeck, M. Morgeneyer, J. Schwedes, D. Kadau, L. Brendel, and D. Wolf, Granular Matter **10**, 285 (2008).
[26] A. D. Araújo, J. S. Andrade Jr., and H. J. Herrmann, Phys. Rev. Lett. **97**, 138001 (2006).
[27] M. K. Kennedy, F. E. Kruis, H. Fissan, B. R. Mehta, S. Stappert, and G. Dumpich, J. Appl. Phys. **93**, 551 (2003).
[28] J. J. Moreau, Eur. J. Mech. A, Solids **13**, 93 (1994).
[29] M. Jean and J. J. Moreau, in *Contact Mechanics International Symposium* (Presses Polytechniques et Universitaires Romandes, Lausanne, 1992), pp. 31–48.
[30] T. Unger and J. Kertesz, in *Modelling of Complex Systems* (American Institute of Physics, Melville, NY, 2003), pp. 116–138.
[31] L. Brendel, T. Unger, and D. Wolf, in *The Physics of Granular Media*, edited by H. Hinrichsen and D. Wolf (Wiley-VCH, Weinheim, 2004), pp. 325–340.
[32] D. Kadau, G. Bartels, L. Brendel, and D. E. Wolf, Phase Transit. **76**, 315 (2003).
[33] A. Taboada, N. Estrada, and F. Radjaï, Phys. Rev. Lett. **97**, 098302 (2006).
[34] V. Richefeu, M. Youssoufi, E. Azéma, and Farhang Radjaï, Powder Technol. **190**, 258 (2009).
[35] D. Kadau, G. Bartels, L. Brendel, and D. E. Wolf, Comput. Phys. Commun. **147**, 190 (2002).

[36] D. Kadau, L. Brendel, G. Bartels, D. Wolf, M. Morgeneyer, and J. Schwedes, in *6th Italian Conference on Chemical and Process Engineering*, Chem. Eng. Trans., vol. 3, edited by S. Pierucci (AIDIC, Milano, Italy, 2003), pp. 979–984.

[37] G. Bartels, T. Unger, D. Kadau, D. Wolf, and J. Kertész, Granular Matter **7**, 139 (2005).

[38] L. Brendel, D. Kadau, D. Wolf, M. Morgeneyer, and J. Schwedes, in *Selected Papers of the Sixth Italian Conference on Chemical and Process Engineering*, AIDIC Conf. Ser., vol. 6, edited by S. Pierucci (AIDIC, Milano, Italy, 2003), pp. 55–66.

[39] M. Morgeneyer, M. Röck, J. Schwedes, L. Brendel, D. Kadau, D. Wolf, and L.-O. Heim, in *Behavior of Granular Media*, Schrif. Mech. Verfahrenstechnik, vol. 9, edited by P. Walzel, S. Linz, Ch. Krülle, and R. Grochowski (Shaker Verlag, Aachen, Germany, 2006), pp. 107–134.

[40] D. Kadau, in *IUTAM ISIMM Symposium on Mathematical Modeling and Physical Instances of Granular Flows, AIP Conference Proceedings, vol. 1227*, edited by J. Goddard, P. Giovine, and J. T. Jenkins (American Institute of Physics, Melville, NY, 2010), pp. 50–57.

[41] P. Meakin, P. Ramanlal, L. M. Sander, and R. C. Ball, Phys. Rev. A **34**, 5091 (1986).

[42] P. Meakin and R. Jullien, Physica A **175**, 211 (1991).

[43] C. Völtz, M. Schröter, G. Iori, A. Betat, A. Lange, A. Engel, and I. Rehberg, Phys. Rep. **337**, 117 (2000).

[44] C. Völtz, W. Pesch, and I. Rehberg, Phys. Rev. E **65**, 011404 (2001).

[45] J. L. Vinningland, O. Johnsen, E. G. Flekkøy, R. Toussaint, and K. J. Måløy, Phys. Rev. E **76**, 051306 (2007).

[46] P. G. Rognon, J.-N. Roux, D. E. Wolf, M. Naaim, and F. Chevoir, Europhys. Lett. **74**, 644 (2006).

[47] S. T. Nase, W. L. Vargas, A. A. Abatan, and J. J. McCarthy, Powder Technol. **116**, 214 (2001).

[48] D. E. Wolf, T. Unger, D. Kadau, and L. Brendel, in *Powders and Grains 2005*, edited by R. Garcia-Rojo, H. J. Herrmann, and S. McNamara (A. A. Balkema, Leiden, Netherlands, 2005), pp. 525–533.

[49] K. Shundyak, M. van Hecke, and W. van Saarloos, Phys. Rev. E **75**, 010301(R) (2007).

[50] L. E. Silbert, Soft Matter **6**, 2918 (2010).

[51] G. R. Farrell, K. M. Martini, and N. Menon, Soft Matter **6**, 2925 (2010).

[52] P. Wang, C. Song, C. Briscoe, K. Wang, and H. A. Makse, Physica A **389**, 3972 (2010).

[53] A. M. Kjeldsen, R. J. Flatt, and L. Bergström, Cement Concrete Res. **36**, 1231 (2006).

[54] G. Lumay and N. Vandewalle, New J. Phys. **9**, 406 (2007).

[55] K. J. Dong, R. Y. Yang, R. P. Zou, and A. B. Yu, Phys. Rev. Lett. **96**, 145505 (2006).

[56] J. M. Valverde and A. Castellanos, Europhys. Lett. **75**, 985 (2006).

[57] R. Son, J. A. Perez, and G. A. Voth, Phys. Rev. E **78**, 041302 (2008).